

Pulse-level control for quantum resource preparation

K. De La Ossa Doria,¹ T. Merlo Vergara,² and D. Goyeneche²

¹*Departamento de Física, Facultad de Ciencias Básicas,
Universidad de Antofagasta, Casilla 170, Antofagasta, Chile*

²*Instituto de Física, Pontificia Universidad Católica de Chile, Casilla 306, Santiago, Chile*

(Dated: February 25, 2026)

Minimizing the time required for quantum state preparation is crucial to mitigate decoherence and enable practical quantum algorithms on near-term hardware. In this work, we introduce a technique for quantum state preparation in transmon-qubit systems using optimized electromagnetic pulse sequences rather than discrete quantum gates. By directly targeting quantum correlations instead of specific target states, we identify minimal-time pulse protocols that optimize relevant entanglement resources, such as concurrence and the three-tangle for two and three qubit systems, respectively. For the figures of merit considered, this approach successfully achieves maximal entanglement in each case: Bell, GHZ and W like states. Beyond state preparation, the resource-oriented nature of the approach leads to a reduced effective expressivity of the control scheme, a feature that represents an advantage in algorithmic settings where excessive control freedom is known to hinder performance.

I. INTRODUCTION

Quantum computing has emerged as one of the most promising paradigms for next-generation information processing technologies. Despite rapid theoretical and experimental advances, the scalable realization of quantum processors remains limited by decoherence, control imperfections, and restricted gate fidelities. To partially overcome these limitations, significant efforts have focused on advanced quantum control techniques aimed at optimizing system dynamics and enabling the precise implementation of quantum states and gates. In particular, quantum optimal control provides a general framework for designing sequences of electromagnetic pulses that maximize the fidelity with respect to target unitary transformations [1–3]. This approach has been successfully applied to effective models describing a wide range of physical platforms, including transmon-type superconducting qubits [4], trapped ions [5], spins in quantum dots [6, 7], and neutral atoms [8], among others.

Among the first algorithms developed in this field are Krotov [9–11] and GRAPE [12, 13], both based on gradient-optimization methods that iteratively refine the control pulses. More flexible approaches such as GOAT [14] enable direct optimization over analytic families of control signals. More recently, machine learning techniques have been incorporated into control design, including deep reinforcement learning [15] and hybrid classical-learning-based strategies [16], expanding the range of physically realizable control protocols. Quantum optimal control plays a central role in physics and chemistry, where precise manipulation of quantum dynamics is required to reach target states, implement unitary operations, or achieve controlled population transfer between specific energy eigenstates [17, 18].

Beyond gate synthesis and state preparation, quantum control is increasingly relevant for the practical implementation of variational quantum algorithms on noisy intermediate-scale quantum [19]. Variational approaches rely on parametrized quantum circuits optimized through

classical feedback, and their performance is strongly influenced by the expressivity of the chosen parametrization [20]. While highly expressive circuits can represent a broad class of quantum states, growing theoretical and numerical evidence indicates that excessive expressivity can induce barren plateau phenomena, where cost-function gradients become exponentially suppressed with system size, rendering optimization impractical [21]. This trade-off between expressivity and trainability highlights the need for control strategies that restrict the accessible dynamical space in a physically informed manner.

From this perspective, pulse-level quantum control provides a natural alternative to standard gate-based constructions. By operating directly on the time-dependent Hamiltonian of the system, pulse-based approaches inherently limit the effective expressivity of the evolution to what is achievable within a given time window and hardware configuration. Rather than being a drawback, this controlled reduction of expressivity can suppress error accumulation, simplify optimization landscapes, and improve robustness and trainability in variational settings, while still enabling the generation of relevant quantum resources.

Recent studies have explored quantum optimal control as a means to manipulate entanglement directly, without relying on fixed gate decompositions or predefined target states. Romano and Del Fabbro [22] analyzed the optimal generation of bipartite entanglement under local control, while Platzer, Mintert, and Buchleitner [23] and Lucas *et al.* [24] formulated dynamical-control frameworks in which multipartite entanglement measures enter explicitly as cost functionals. Complementary pulse-based and variational approaches have demonstrated efficient entanglement generation under realistic constraints in superconducting and hybrid architectures [22, 23], providing a solid foundation for quantum resource-oriented pulse optimization.

In this work, we focus on identifying the simplest possible set of electromagnetic pulse protocols that generate a

prescribed set of quantum correlations. By emphasizing the preparation of quantum resources rather than reproducing predefined quantum states, our approach substantially reduces the control cost required to achieve a given level of entanglement. We illustrate the method by considering minimal two- and three-qubit systems and designing pulse sequences that directly optimize resource-oriented objectives: (a) for two qubits, the maximization of quantum negativity; and for three qubits, (b) the maximization of the three-tangle, and (c) the minimization of the cost function $\sqrt{\sum_{i<j} (C_{ij} - \frac{2}{3})^2}$, $i, j = 1, 2, 3$, where C_{ij} denotes the concurrence of the bipartite reduction ρ_{ij} [25]. These representative cases define fundamental control primitives that can be systematically extended to construct less expressive, resource-efficient pulse-based implementations of more general quantum circuits.

II. SUPERCONDUCTING QUBITS

Superconducting circuits constitute one of the most versatile platforms for the physical realization of quantum bits. They enable precise control of quantum states through microwave pulses applied to nonlinear resonant elements operating at cryogenic temperatures [26, 27]. Among the different implementations, the transmon qubit has become a standard architecture due to its long coherence time, high-fidelity gate operations, and a simple integration into scalable multi-qubit [28]. These systems can be accurately modeled as weakly anharmonic oscillators, where quantum information is encoded in the two lowest energy levels of the circuit.

The dynamics of an n -qubit superconducting processor driven by external control fields is governed by a time-dependent Hamiltonian that can be expressed as

$$H(t) = H_{\text{sys}} + \sum_{i=1}^n \mu_i(t) H_i, \quad (1)$$

where H_{sys} represents the intrinsic (drift) Hamiltonian of the system, and the second term corresponds to the set of control Hamiltonians H_i modulated by time-dependent amplitudes $\mu_i(t)$. These control fields are typically implemented as shaped microwave pulses that induce transitions between energy levels or generate effective couplings between qubits. The objective of optimal control is to determine the set of functions $\{\mu_i(t)\}$ and their parameters that drive the system from an initial state $|\psi_0\rangle$ to a target state $|\psi_t\rangle$, maximizing a cost functional $\mathcal{F}[\mu_i(t)]$ associated with fidelity, entanglement, or other physical figure of merit.

The explicit form of the Hamiltonian depends on the system dimensionality and on whether the analysis addresses single-qubit dynamics or coupled multi-qubit configurations. In what follows, we present the effective Hamiltonians for one, two, and three transmon qubits, focusing on the introduction of control terms that enable

the implementation of local operations and entangling interactions.

1. Single Qubit

The Hamiltonian of a single superconducting qubit can be written as [4]:

$$H_{1,\text{sys}} = \omega b^\dagger b + \frac{\alpha}{2} b^\dagger b^\dagger b b, \quad (2)$$

where ω denotes the transition frequency between the two lowest energy levels $|0\rangle \leftrightarrow |1\rangle$, α is the anharmonicity factor, and b (b^\dagger) is the annihilation (creation) operator of the transmon mode. Here, and along the entire work, we assume that $\hbar = 1$. The weak anharmonicity ensures sufficient separation between the first and second excited states, allowing the system to operate effectively as a two-levels system while retaining an accurate description of higher levels, when necessary.

The transmon state is manipulated through an external electromagnetic drive pulse, having frequency ω_d , whose interaction with the circuit can be modeled as

$$H_{1,\text{ctl}}(t) = \Omega_d \text{Re}[\mu(t) e^{i\omega_d t} (b^\dagger + b)], \quad (3)$$

where Ω_d represents the drive strength and $\mu(t)$ is a dimensionless control envelope normalized to the interval $\mu(t) \in [-1, 1]$. The drive Hamiltonian describes the coherent coupling between the qubit and the microwave field that implements state rotations in the Bloch sphere.

For a simplified mathematical description of the problem it is convenient to move into a *rotating reference frame* at the drive frequency ω_d and apply the rotating-wave approximation (RWA) [4] [17, 18]. This transformation removes fast-oscillating terms and leads to an effective Hamiltonian expressed as

$$H_{\text{RWA}} = \frac{\Delta}{2} \sigma_z + \frac{\Omega_d}{2} [\text{Re}\{\mu(t)\} \sigma_x + \text{Im}\{\mu(t)\} \sigma_y], \quad (4)$$

where $\Delta = \omega - \omega_d$ is the detuning between the qubit and drive frequencies, and $\sigma_x, \sigma_y, \sigma_z$ are the Pauli matrices. This effective Hamiltonian captures the essential dynamics of single-qubit control, where the envelope $\mu(t)$ directly determines the rotation axis on the Bloch sphere.

2. Two qubits

In this configuration, we consider a system composed of two capacitively coupled transmon qubits, each characterized by intrinsic physical parameters such as the transition frequency and the anharmonicity. The energy levels of each qubit can be individually manipulated by applying microwave pulses through independent control channels. When the drive frequency is tuned in resonance with the desired transition frequency of a given qubit, and the pulse amplitude, phase, and temporal shape are

appropriately modulated, precise local gates can be implemented with high fidelity [29].

The implementation of two-qubit operations relies on dynamically modulating the interaction between the transmons. This can be achieved by applying an additional off-resonant drive to one of the qubits, whose frequency is chosen to activate a specific coupling channel with the target qubit. Under this driving scheme, the effective Hamiltonian describing the coupled system is given by

$$H_{2,\text{sys}} = \sum_{i=0}^1 \left(\omega_i b_i^\dagger b_i + \frac{\alpha_i}{2} b_i^\dagger b_i^\dagger b_i b_i \right) + J_{01} \left(b_0 b_1^\dagger + b_0^\dagger b_1 \right), \quad (5)$$

where ω_i denotes the transition frequency between the first two levels of the i th qubit, α_i is its anharmonicity, and J_{01} is the coupling strength between the two transmons. The operators b_i (b_i^\dagger) are the annihilation (creation) operators acting on each local Hilbert space.

The control Hamiltonian associated with the external drives can be expressed as

$$H_{2,\text{ctrl}}(t) = \sum_{j=0}^1 \Omega_{d_j} \text{Re} \left[\mu_j(t) e^{-i(\omega_{d_j} t + \phi_j)} \right] (b_j^\dagger + b_j), \quad (6)$$

where Ω_{d_j} is the drive amplitude for the j th qubit, ω_{d_j} the drive frequency, ϕ_j the drive phase, and $\mu_j(t)$ the normalized control envelope. By tuning these parameters, both local and nonlocal interactions can be engineered, enabling the implementation of high-fidelity entangling gates such as the controlled-phase or iSWAP gates, depending on the specific detuning and pulse conditions.

3. Three qubits

We now extend the model to a system of three transmon qubits, labeled from right to left as 0, 1, and 2. In this configuration, qubit 0 acts as a control for qubit 1, while qubit 1 controls qubit 2, resulting in a linear, unidirectional coupling topology. Although the qubits are physically connected, bidirectional control is not assumed. The system Hamiltonian is given by

$$H_{3,\text{sys}} = \sum_{i=0}^2 \left(\omega_i b_i^\dagger b_i + \frac{\alpha_i}{2} b_i^\dagger b_i^\dagger b_i b_i \right) + J_{01} \left(b_0 b_1^\dagger + b_0^\dagger b_1 \right) + J_{12} \left(b_1 b_2^\dagger + b_1^\dagger b_2 \right), \quad (7)$$

where ω_i , α_i , and J_{ik} denote the transition frequency, anharmonicity, and coupling strength, respectively, for each pair of interacting qubits. The ladder operators b_i (b_i^\dagger) act locally on their corresponding subspaces.

As in the two-qubit case, the transmons are individually controlled by microwave pulses applied to each qubit

through dedicated drive lines. The corresponding control Hamiltonian reads

$$H_{3,\text{ctrl}}(t) = \sum_{i=0}^2 \Omega_{d_i} \text{Re} \left[\mu_i(t) e^{i\omega_{d_i} t} \right] (b_i^\dagger + b_i), \quad (8)$$

where Ω_{d_i} , $\mu_i(t)$, and ω_{d_i} represent the drive amplitude, control envelope, and drive frequency for each qubit, respectively. As before, local gates can be implemented by applying resonant pulses at the corresponding transition frequencies through independent control channels, while for two-qubit gates the implementation consists of sending a pulse to one of the qubits (control qubit) at the frequency of the qubit to be controlled (target qubits).

The central challenge of this work consists in determining the optimal set of pulse parameters—amplitudes, durations, and relative phases—that yield the target entangled states representative of each inequivalent class of multipartite entanglement, where optimality is in the sense of minimizing the total state preparation time. This optimization problem is highly nontrivial due to the large number of variables involved and complexity of the problem itself, requiring careful treatment to identify physically feasible solutions.

III. IMPLEMENTATION

A. Three-qubit setup

An optimal quantum control scheme was implemented to prepare tripartite entangled states—specifically the GHZ and W classes—in a system of three superconducting transmon qubits. The physical parameters were extracted from the simulated backend *Fake_Sherbrooke* provided by IBM Quantum, which reproduces the Hamiltonian characteristics of the real *ibm_sherbrooke* device. This processor belongs to the *Eagle* family of 127-qubit chips and features a hexagonal lattice connectivity, where each qubit is coupled to two or three neighbors. Such a layout reduces undesired crosstalk and supports high-fidelity native operations. The architecture natively implements a standard instruction set including ECR, ID, DELAY, MEASURE, RESET, RZ, SX, X, IF_ELSE, FOR_LOOP, and SWITCH_CASE gates [30].

The system dynamics were simulated using the *Solver* module of `qiskit_dynamics` (version 0.5.1), with the differentiable integrator `jax_odeint`. This method provides efficient and accurate time evolution for systems governed by time-dependent Hamiltonians, even when multiple control channels are present. A key advantage of `jax_odeint` is its adaptive-step integration scheme: unlike explicitly discretized methods, it automatically adjusts the time grid according to the local complexity of the evolution, allowing the capture of fast or strongly driven dynamics without manual specification of sam-

pling points. Numerical precision and stability are ensured by user-defined absolute and relative tolerances.

The physical model considered consists of three linearly coupled transmon qubits with natural frequencies $\omega_7 \approx 29.877$ GHz, $\omega_8 \approx 30.235$ GHz, and $\omega_9 \approx 29.135$ GHz; anharmonicities $\Delta_7 \approx -1.954$ GHz, $\Delta_8 \approx -1.969$ GHz, and $\Delta_9 \approx -1.839$ GHz; coupling strengths $J_{78} \approx 0.013$ GHz and $J_{89} \approx 0.014$ GHz; and drive amplitudes $\Omega_{d_0} \approx 0.396$ GHz, $\Omega_{d_1} \approx 0.650$ GHz, and $\Omega_{d_2} \approx 4.638$ GHz. These parameters were obtained directly from the backend's Hamiltonian specification using the `qiskit` package (version 1.1.0). The total Hamiltonian, including drift, interaction, and control terms, was constructed according to Eqs. (7) and (8).

Control fields were generated through the `qiskit.pulse` module as piecewise-constant microwave drives applied via the channels $d0$, $d1$, $d2$, $U0$, and $U1$. Each pulse was characterized by two main attributes—duration and amplitude—allowing the control sequence to be expressed as a sum of constant-amplitude segments. These signals define a set of time-dependent functions $\mu_j(t)$ whose temporal support spans the total integration window T . The simulation time was expressed as an integer multiple of the backend's native time resolution $dt = 2.2222$ ns, corresponding to the minimum pulse-sampling interval.

The optimization of the control parameters was carried out using the *Differential Evolution* algorithm, a population-based global search technique particularly suitable for nonconvex objective landscapes, as commonly encountered in quantum optimal control. This method explores the parameter space extensively and avoids premature convergence to local minima. The cost function $\mathcal{F}[\mu(t)]$ was defined in terms of the normalized final state of the system and tailored to the specific tripartite state to be prepared. Distinct target metrics were employed for the GHZ and W classes, enabling flexible adaptation of the optimization routine to the desired form of multipartite entanglement. This formulation provides a unified numerical framework for pulse-based generation of genuinely tripartite entangled states in superconducting architectures.

IV. RESULT

A. Bipartite entanglement

In this work, we consider a control scheme based on the application of two local pulses on qubits 0 and 1, with equal durations but independent amplitudes. A resonant pulse is then applied to qubit 0, tuned to the transition frequency of qubit 1, thereby inducing an effective controlled interaction between the two qubits, as shown in Figure. (1). A total of five parameters were optimized: the amplitudes and duration of each local pulse,

together with the parameters of the control pulse. As an objective function, we use the *negativity*, a bipartite entanglement measure that reaches its maximum value for Bell-type states. With this proposal, we achieve a negativity of $\mathcal{N}(\rho_{01}) \approx 0.499$ for two-qubit maximally entangled states. The state obtained with this approach is given by:

$$|\Psi\rangle = (-0.3684480152 + 0.5999791316i)|00\rangle - (0.0383474023 - 0.0330939344i)|01\rangle - (0.0167077292 + 0.0291402261i)|10\rangle + (0.2125136408 + 0.6748444424i)|11\rangle. \quad (9)$$

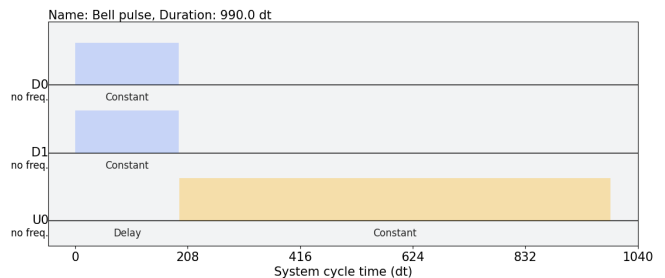


Figure 1. (color online) Pulse scheme required to prepare the maximally entangled state eq. (9). The scheme shows two local pulses (cyan) applied to qubits 0 and 1 (channels D0 and D1, respectively). Afterwards, a pulse is sent to qubit 0 (channel U0, yellow pulse) with frequency of qubit 1 (target qubit) in order to produce entanglement. The diagram shows that the duration of entire pulse sequence is 989.0 dt

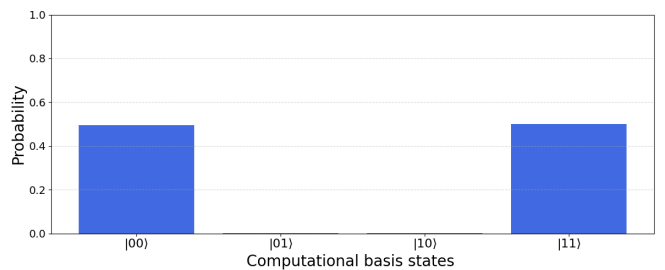


Figure 2. Probability distribution of the state eq. (9) in the computational basis, where we can show large populations in the states $|00\rangle$ and $|11\rangle$. This state exhibit a nearly maximal value of negativity $\mathcal{N}(\rho_{01}) = 0.499$.

In the above described two-qubit implementation, we assumed that the system can be described effectively by a two-level model, under the approximation that the third energy level is sufficiently far detuned, so that the probability of undesired excitation to higher levels is negligible. Nevertheless, in realistic physical systems the presence of the third level cannot be ignored, since population leakage to this level may occur. For this reason, we consider a three-level model, using the

parameters described in eqs. (5) and (6), as well as in Section III.

In this case, we use the same pulse sequence as in the previous implementation, with the difference that the pulses are modeled using Gaussian Square functions, which allows us to capture the system dynamics more realistically (see Fig. 3). The characteristic parameters of this function are the amplitude (A), the width, the standard deviation (σ), and the duration, which are detailed in Appendix B. This sequence allows us to obtain a locally unitary (LU) version of the Bell state, with negativity $\mathcal{N}(\rho_{01}) = 0.499$. For this implementation, the obtained state is given by:

$$\begin{aligned} |\Psi_{gauss}\rangle = & (0.52524396)|00\rangle \\ & + (0.15611769 - 0.44623461i)|01\rangle \\ & + (-0.47909249 + 0.001467147i)|10\rangle \\ & + (-0.20785354 - 0.47737390i)|11\rangle \end{aligned} \quad (10)$$

It is worth noting that the widths of the Gaussian Square functions were fixed using the square pulses obtained in figure 1. In this way, it was only necessary to optimize the σ parameters of each function. As a result of the evolution, the final state vector is described by 27 components. Afterwards, those associated with the third level were removed, the state was re-normalized, and the cost function was minimized to determine the optimal parameters.

Finally, the population probabilities of the state vector were computed using the optimal parameters obtained. The results are presented in Fig. (4), where one observes that the achieved populations take very similar values.

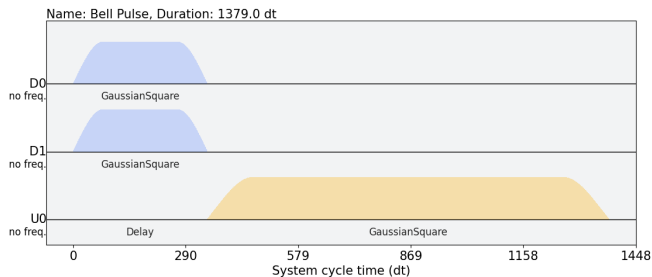


Figure 3. Gaussian Square pulse scheme used to obtain a Bell-type state between qubits zero and one, considering three energy levels. The pulse widths were previously adjusted from those obtained in the square-pulse case, figure (1). In this way, only the amplitude and σ parameters were varied, where σ indicates the smoothness of the envelope edges. The diagram also shows that the execution time is 1379.0 dt .

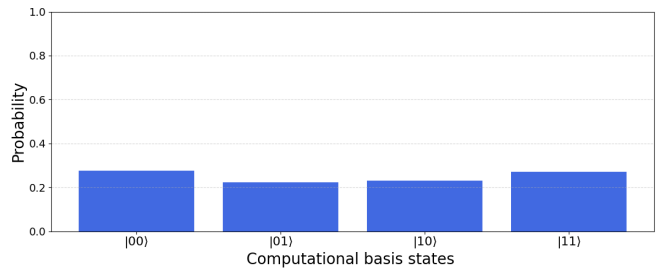


Figure 4. Probability distribution in the computational basis for the two-qubit state eq. (10). This distribution is obtained by applying the pulse sequence of Figure (3) and keeping the first two levels per system, so that we consider two qubits. Here, negativity achieves the value $\mathcal{N}(\rho_{01}) = 0.499$.

B. Tripartite entanglement

In three-qubit systems, entanglement splits into inequivalent SLOCC classes [31]. Here, we use optimal pulse control to prepare states in each class. For a given target class, we optimize the pulse parameters so that the final state is locally unitary (LU) equivalent to the corresponding canonical representative. In what follows, we outline the optimization procedure and report the results obtained for each entanglement class.

Beyond the SLOCC viewpoint, three-qubit states can also be classified using invariant quantities. These invariants are algebraic functions of the computational-basis coefficients and remain unchanged under local unitary (LU) transformations. They provide a direct way to identify the entanglement family without explicitly converting the state to a canonical form. A key example is the 3-tangle [32], it is nonzero only for the GHZ-class and vanishes for the W-class. In our analysis, we use such invariants to validate the output of the pulse optimization by comparing their values with those of the canonical representative of each target class.

1. GHZ state

For preparing a Greenberger–Horne–Zeiling (GHZ) class state in our system, we design a coherent microwave pulse protocol. The pulse scheme, shown in Fig. 5, consists of five constant-amplitude pulses: three local drive pulses applied on the drive channels (D0, D1, D2) and two cross-frequency control pulses (U0, U1). Each pulse is defined by its amplitude and duration, which are optimized to maximize the generation of tripartite entanglement.

The sequence starts with two simultaneous drive pulses on qubits 0 and 1 (channels D0 and D1), with identical duration, which initializes their coherent dynamics. Next, a control pulse is applied on channel U0, corre-

sponding to driving qubit 0 at the resonance frequency of qubit 1. This cross-frequency coupling builds correlations between qubits 0 and 1.

In the second stage, the third qubit is activated by a local drive pulse on channel D2. The sequence ends with a control pulse on channel U1, applied to qubit 1 at the resonance frequency of qubit 2. This final pulse mediates the interaction between the previously correlated pair (0–1) and qubit 2, extending the correlations into the tripartite regime characteristic of GHZ-class states.

The control parameters are optimized through an optimal-control search over the parameter space, using the *three-tangle* (τ_3) as the cost function. This quantity measures genuine three-qubit entanglement and approaches its maximum value for the GHZ state. In our implementation, the maximal value for the 3-tangle yields $\tau_3 \approx 0.999$, which makes it an effective guide toward the target state.

Using the pulse configuration above introduced, we obtain the probability distribution shown in Fig. 6. The dominant populations here correspond to $|000\rangle$ and $|111\rangle$, while the remaining basis states contribute weakly. This indicates a predominantly coherent superposition of $|000\rangle$ and $|111\rangle$. Small deviations from the ideal distribution reflect practical limitations of calibration and optimization, while preserving the genuinely tripartite nature of the generated entanglement.

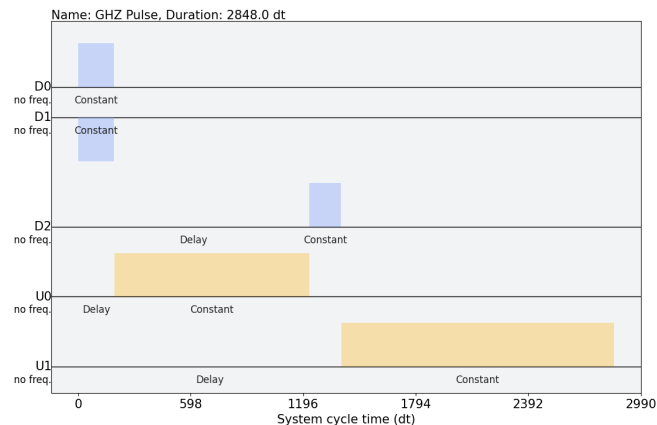


Figure 5. Square-pulse scheme used to generate the GHZ state. Three local pulses (cyan) are applied on channels D0, D1, and D2, and two cross-frequency pulses (yellow) are applied on channels U0 and U1. The U0 pulse is sent to qubit 0 at the resonance of qubit 1, and the U1 pulse is sent to qubit 1 at the resonance of qubit 2, enabling the required correlations. It can be observed that the duration of the entire pulse pattern is 2848.0 dt .

With the sequence of pulses depicted in Figure 5, we obtain the following physically implemented GHZ state:

$$\begin{aligned}
 |\Psi'_{GHZ}\rangle = & (0.66802070) |000\rangle \\
 & + (0.05252552 + 0.13434712 i) |001\rangle \\
 & + (-0.10755963 + 0.03577012 i) |010\rangle \\
 & + (-0.11451824 + 0.07573796 i) |011\rangle \\
 & + (-0.03285393 - 0.11985692 i) |100\rangle \\
 & + (-0.06979810 - 0.10802873 i) |101\rangle \\
 & + (0.11835156 - 0.10244015 i) |110\rangle \\
 & + (-0.65590019 - 0.12061437 i) |111\rangle.
 \end{aligned} \tag{11}$$

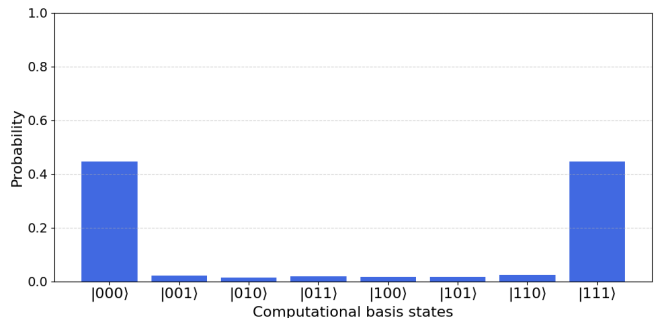


Figure 6. Probability distribution obtained from the pulse scheme in Fig. (9). The achieved three-tangle is $\tau_3 \approx 0.999$. The dominant populations correspond to $|000\rangle$ and $|111\rangle$, while the other populations are present but small.

As well as for two-transmons, we consider now a more realistic model with three energy levels per individual system. In this case, we solve the time-dependent Schrödinger equation using the pulse scheme shown in Fig. (7). Each pulse is modeled with a Gaussian-Square envelope, using the square-pulse scheme of Fig. (5) as a reference: the widths of the square pulses are reused as parameters for the Gaussian pulses. In this setting, we optimize both the pulse amplitudes and the standard deviation σ , again using the three-tangle as the cost function.

Since a three systems with three levels per site evolves in a 27-dimensional state vector, at the end of the dynamics we restore the three transmon state by discarding entries associated with the third level for each qubit. We then renormalize the state and evaluate the cost function. As a result, we obtain a three-tangle $\tau_3 \approx 0.999$.

The probability distribution of the resulting state is shown in Fig. (8). We observe four basis states with significant populations, indicating the emergence of near-equiprobability within certain pairs. This shows that, even in the presence of additional levels, the proposed protocol still generates high-quality tripartite entanglement, supporting the robustness of the approach.

The state obtained for the previous configuration is the following, together with its corresponding probability distribution.

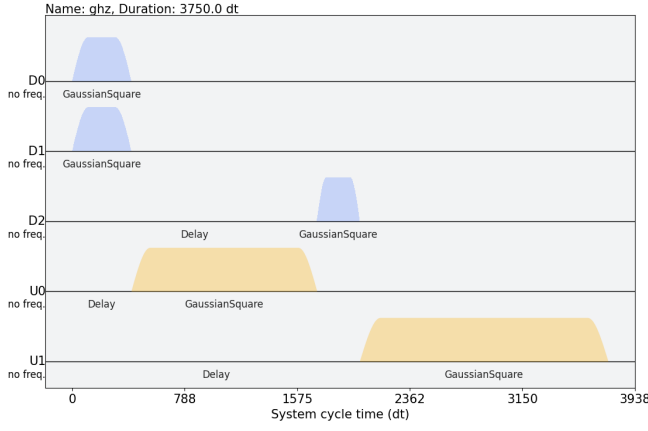


Figure 7. Pulse scheme used to generate the GHZ state when three levels are considered for each qubit. The sequence includes three local pulses (cyan) and two cross-frequency pulses (yellow): the local pulses act on channels D0, D1, and D2, while the cross pulses act on channels U0 and U1. The parameters are optimized by maximizing the three-tangle. The widths of the Gaussian pulses are set from the corresponding square pulses; therefore, amplitude (A) and standard deviation (σ) are the optimization parameters, for each pulse. It is observed that the total duration of the pulse scheme is 3750.0 dt .

$$\begin{aligned}
 |\Psi'_{GHZ_gauss}\rangle = & (0.083077001) |000\rangle \\
 & + (-0.27443508 - 0.49890668 i) |001\rangle \\
 & + (-0.015364393 + 0.40749508 i) |010\rangle \\
 & + (-0.037686058 - 0.045737665 i) |011\rangle \\
 & + (-0.050473366 - 0.030457922 i) |100\rangle \\
 & + (0.16998902 - 0.36956385 i) |101\rangle \\
 & + (-0.44943589 - 0.34799860 i) |110\rangle \\
 & + (-0.075711212 + 0.036034076 i) |111\rangle.
 \end{aligned} \tag{12}$$

2. W state

In order to efficiently prepare a three-qubit W state we design the coherent pulse protocol shown in Fig. (9). The sequence considers constant-amplitude pulses applied on the local drive channels and on the cross-frequency control channels (U0, U1). Each pulse is defined by its amplitude and duration, both of them optimized for each pulse.

The sequence of pulses starts by driving the three qubits through local pulses on channels D0, D1, and D3, generating initial coherence in the subsystem. We then activate the coupling between qubits 0 and 1 through a control pulse on channel U0, which implements a cross-frequency resonant interaction.

In the second stage, we apply three local drive pulses

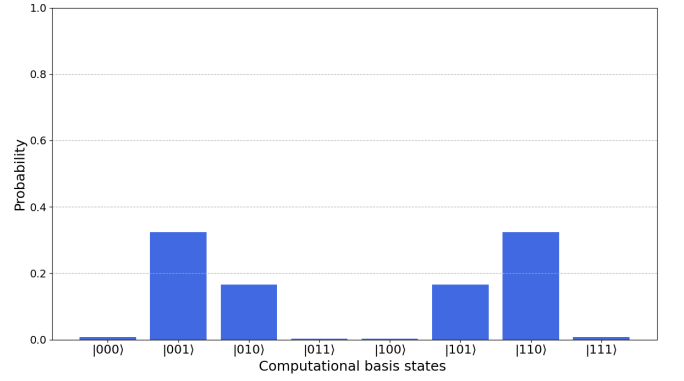


Figure 8. Probabilities of the state obtained by optimizing the pulse scheme in Fig. (7). The plot shows that $|001\rangle$ and $|110\rangle$ have nearly the same population, and likewise for $|010\rangle$ and $|101\rangle$.

again on D0, D1, and D2; next, a pulse is applied on channel U1 to couple qubits 1 and 2, thereby extending the correlations to qubit 0. Finally, three additional local pulses are applied on D0, D1, and D2, and the sequence ends with a pulse on channel U0 to reinforce the coupling between qubits 0 and 1. The optimization target are the squared concurrences between qubit pairs reaching the theoretical value $\frac{4}{9}$ as the cost function, the best approximation to a state equivalent to W given by this cost function is:

$$\begin{aligned}
 |\Psi'_W\rangle = & (0.51397601) |000\rangle \\
 & + (-0.10295038 + 0.20024143 i) |001\rangle \\
 & + (-0.17617122 - 0.12098743 i) |010\rangle \\
 & + (0.30108107 - 0.16458899 i) |011\rangle \\
 & + (-0.20955602 - 0.12563232 i) |100\rangle \\
 & + (-0.35878680 + 0.39267187 i) |101\rangle \\
 & + (0.17604487 + 0.13212849 i) |110\rangle \\
 & + (-0.30967882 + 0.18642040 i) |111\rangle.
 \end{aligned} \tag{13}$$

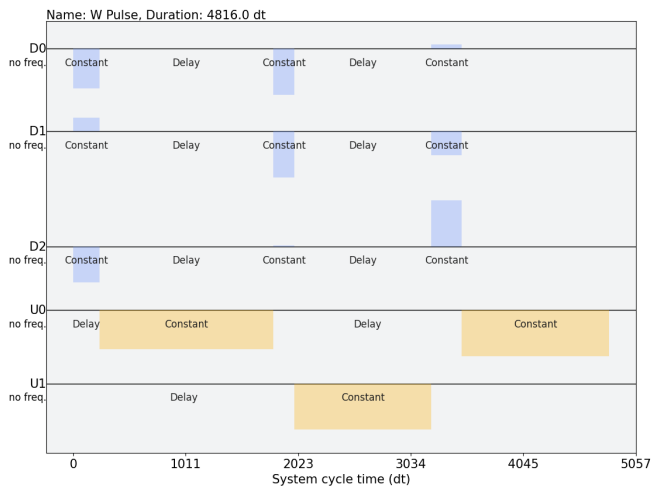


Figure 9. Pulse scheme used to obtain a W state in the two-level model. The sequence consists of 9 local pulses (cyan) and three cross-resonance pulses (yellow). It starts with three local pulses of equal duration on channels D0, D1, and D2, followed by a cross-resonance pulse on channel U0; then three local pulses of equal duration are applied, followed by a cross pulse on channel U1; next, another set of three local pulses of equal duration is applied, and the sequence ends with a cross pulse on channel U1. Note that the cross pulses generate the correlations between the qubits. The figure shows that the duration of the entire scheme is 4816.0 dt .

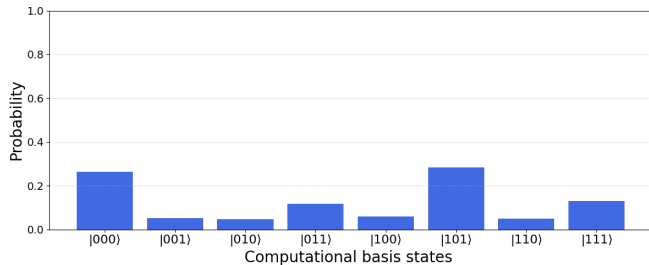


Figure 10. Probability distribution obtained by applying the pulse sequence of Fig. 9. All populations are lifted, with larger weights on $|000\rangle$ and $|001\rangle$. The resulting squared concurrences are $\mathcal{C}^2(\rho_{01}) = 0.442$, $\mathcal{C}^2(\rho_{02}) = 0.444$, and $\mathcal{C}^2(\rho_{12}) = 0.442$.

Sq. Conc.	Value
$\mathcal{C}^2(\rho_{01})$	0.444
$\mathcal{C}^2(\rho_{02})$	0.442
$\mathcal{C}^2(\rho_{12})$	0.442

Table I. Squared concurrences for the W state optimization.

These results in the table I show that each bipartition exhibits nearly the same amount of quantum correlation. This is a hallmark of W-class entanglement, where losing one qubit does not destroy the correlations among the remaining qubits.

As a result of the protocol, we obtain the probability distribution shown in Fig. 10. We observe a high population in the states $|000\rangle$ and $|101\rangle$, followed by nearly equal populations in $|011\rangle$ and $|111\rangle$. The remaining populations are smaller and can be attributed to unwanted coupling effects in the system. The comparison of the squared concurrences with the ideal case is reported in Table I.

Squared concurrence	W_{num}	W_{ide}	Error (%)
$\mathcal{C}^2(\rho_{01})$	0.444	0.444	0.032
$\mathcal{C}^2(\rho_{02})$	0.442	0.444	0.505
$\mathcal{C}^2(\rho_{12})$	0.442	0.444	0.550

Table II. Comparison between the squared concurrences of the obtained state and the ideal W state.

In addition to Table II, we perform an independent validation using the Bures metric to find local unitary transformations that map the numerically obtained state to an ideal W state. The parameters of the three local unitaries are determined by optimization, using the Bures distance as the cost function, which quantifies how close the numerical state is to the ideal W state. The optimization is performed in two stages: we first use the global optimizer *differential evolution*, and then refine the result by having a fine tuning control with *Nelder-Mead*. The final Bures distance between these states is $D_B = 1.3 \times 10^{-5}$, confirming the high fidelity of the achieved result.

To complete the study, we consider a system of three transmon with three levels. The dynamics is obtained by integrating the time-dependent Schrödinger equation using the pulse scheme shown in Fig. (11). Here the implemented pulses are Gaussian Square envelopes, arranged in the same pattern as the square pulses shown in Fig. (9). Therefore, the width of each Gaussian pulse is fixed from the previously optimized duration of the square pulses, while the free parameters are the amplitudes and the σ values for each pulse.

In this implementation, we explicitly simulate the three levels of each transmon and then project the final state onto the two-level subspace, followed by renormalization, before evaluating the cost function.

With this configuration, we obtain the following squared concurrence shown in Table III:

Sq. Conc.	Value
$\mathcal{C}^2(\rho_{01})$	0.441
$\mathcal{C}^2(\rho_{02})$	0.435
$\mathcal{C}^2(\rho_{12})$	0.435

Table III. Squared concurrence values obtained in the optimization of the W state for the Gaussian Square implementation.

These values reveal a close approach to the theoretical W-state benchmark. Figure 13 shows that the final probability distribution is concentrated on six of the eight

computational basis states, with larger weights on $|011\rangle$ and $|110\rangle$. This provides clear evidence that the protocol generates a W -like quantum state.

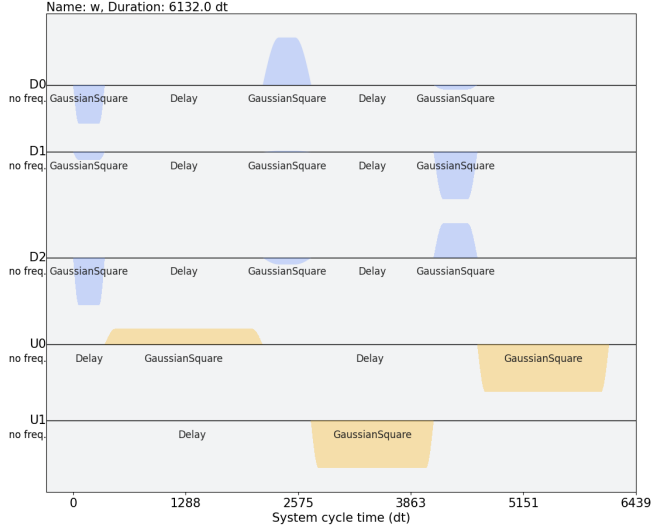


Figure 11. Pulse scheme used to obtain a state equivalent to W . The sequence includes 12 Gaussian Square pulses, where nine are local (light blue) and three are cross-resonance pulses. The width of each pulse is set from the square-pulse results (see Figure). The optimized parameters are the amplitude of each pulse and σ , which controls the edge smoothness of each envelope. The total duration of the pulse scheme was 6132.0 dt .

The state obtained using the pulse scheme of Figure 11 is the following one:

$$\begin{aligned}
 |\Psi'_{w_gauss}\rangle = & (0.07380426) |000\rangle \\
 & + (0.42636680 - 0.11662020 i) |001\rangle \\
 & + (0.23181399 - 0.14600679 i) |010\rangle \\
 & + (-0.33601067 + 0.39076550 i) |011\rangle \\
 & + (-0.02962331 - 0.04744894 i) |100\rangle \\
 & + (-0.24675065 - 0.28302861 i) |101\rangle \\
 & + (-0.39841893 - 0.29674605 i) |110\rangle \\
 & + (-0.25847184 - 0.02799731 i) |111\rangle.
 \end{aligned} \tag{14}$$

State	Gates scheme	t_{gates}	square pulse scheme	t_{pulses}
Bell	Figure 15	2912 dt	Figure 3	1379.0 dt
GHZ	Figure 17	5315 dt	Figure 7	3750.0 dt
W	Figure 19	8224 dt	Figure 11	6132.0 dt

Table IV. Execution time of sequence of gates required to implement some emblematic quantum states (Bell, GHZ, W) compared with time required to implement our pulse schemes achieving the same quantum correlations of those states. That is, the pulse schemes differ at most in local unitary operations with respect to the reference states. Both scheme times, gates and pulses, are taken from the `ibm_sherbrooke` quantum processor, where the discrete time (dt) step is given by $dt = 2.2222$ ns. Here, pulses are modeled by using Gaussian square functions.

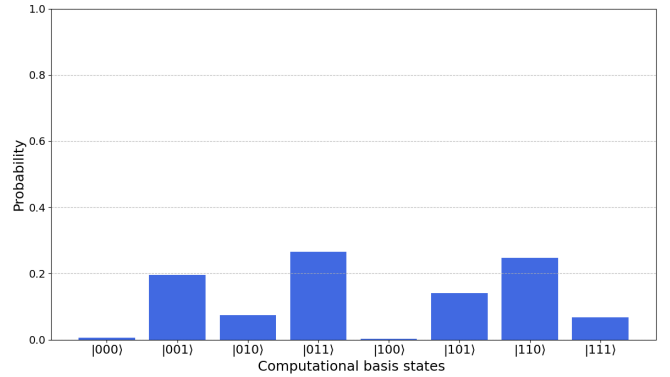


Figure 12. Probability distribution of the state (14) obtained by using the pulse scheme in Fig. 11

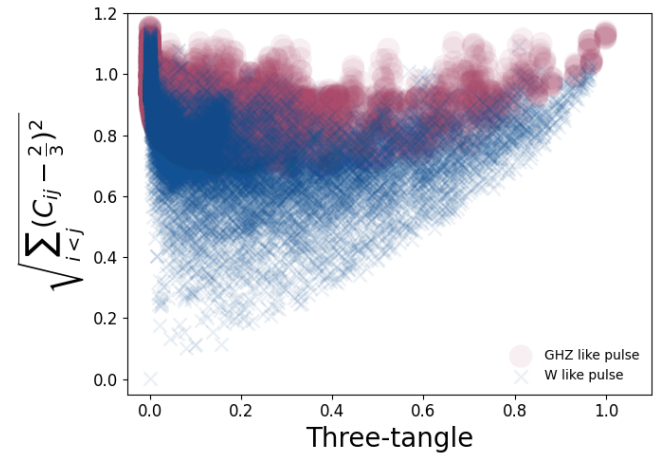


Figure 13. Graphical representation of the cost function $\sqrt{\sum_{i<j} (C_{ij} - \frac{2}{3})^2}$, $i, j = 1, 2, 3$, where C_{ij} denotes the concurrence of the bipartite reduction ρ_{ij} , vs. the three tangle τ . The GHZ and W classes are depicted in purple (circles) and blue (crosses), respectively. Visualized correlations are those that can be implemented with the pulses schemes from Figures 5 and 9, when varying the amplitude and length of each pulse.

V. DISCUSSION

The results presented in this work demonstrate that optimized electromagnetic pulse sequences provide a viable and efficient alternative to gate-based strategies for quantum state preparation in superconducting architectures. By directly targeting entanglement measures rather than specific target states, the proposed approach significantly reduces the control overhead and total evolution time required to generate relevant quantum correlations.

This reduction in the effective expressivity of the control scheme plays a crucial role in mitigating error propagation and decoherence effects. By restricting the accessible dynamical pathways to those strictly required for generating a given quantum resource, the accumulation of control imperfections across long gate sequences is naturally suppressed. Beyond noise mitigation, reduced expressivity also offers an important advantage for practical applications: simpler control landscapes are known to alleviate optimization difficulties in variational quantum algorithms. In particular, limiting circuit expressivity has been shown to establish an upper bound for the barren plateau phenomena, where gradients vanish exponentially with system size [20]. In this context, it is worth emphasizing that variational algorithms formulated directly at the pulse level—replacing logical gates by optimized electromagnetic controls—have already been successfully implemented in superconducting platforms [19, 22, 33–36].

A notable feature of the proposed methodology is that the resulting pulse schemes are substantially shorter than those obtained by compiling standard quantum circuits into native gates. Even in the absence of decoherence modeling, this reduction in total duration is relevant, as it establishes a lower bound on the control time required to access specific entanglement resources. These findings suggest that pulse-level state preparation may offer a practical route to mitigate decoherence effects in near-term superconducting processors.

From a broader perspective, the results support the idea that quantum optimal control can be naturally formulated at the level of quantum resources rather than unitary gates. By focusing on entanglement measures as optimization targets, the approach bypasses unnecessary constraints associated with circuit decompositions and opens the possibility of exploring otherwise inaccessible regions of the state space within realistic hardware limitations.

VI. CONCLUSIONS

In this work, we have investigated quantum state preparation in superconducting transmon systems using

optimized electromagnetic pulse sequences, moving beyond conventional gate-based paradigms. By directly optimizing entanglement measures, we have shown that both bipartite and multipartite quantum correlations can be efficiently generated with short, physically feasible control protocols.

For two-qubit systems, pulse sequences maximizing negativity yield states locally equivalent to maximally entangled Bell states, maintaining their performance even when higher transmon levels are included. For three-qubit systems, we demonstrated the preparation of states belonging to the GHZ and W entanglement classes, using cost functions tailored to genuine tripartite correlations and balanced bipartite entanglement, respectively.

The results highlight the advantages of pulse-level optimization as a resource-oriented approach to quantum state engineering. In particular, the reduced execution times obtained in comparison with transpiled circuit implementations indicate that such strategies may play an important role in mitigating decoherence in current and future superconducting quantum devices.

Beyond state preparation, the results presented in this work are directly relevant to the implementation of variational quantum algorithms on superconducting platforms. By operating at the pulse level and explicitly reducing the effective expressivity of the control scheme, the proposed approach naturally constrains the accessible region of the parameter landscape. Such restrictions are known to improve trainability by mitigating barren plateau phenomena, which arise when highly expressive parametrized circuits exhibit exponentially suppressed gradients. In this sense, pulse-based variational formulations provide a physically motivated mechanism to balance expressivity and optimization stability, suggesting that resource-oriented pulse control may play a key role in scalable variational algorithms on near-term quantum hardware.

Looking forward, the framework presented here can be extended to larger systems, different hardware architectures, and more complex resource measures. Incorporating decoherence models, robustness constraints with respect to Hamiltonian parameter uncertainties and control-amplitude fluctuations, and experimental calibration feedback constitutes a natural next step toward the experimental realization of resource-driven quantum state preparation protocols.

Acknowledgements We kindly acknowledge valuable comments from Herbert Díaz Moraga. We acknowledge grant FONDECYT Regular nr 1230586, Chile. KDD belongs to the PhD program *Doctorado en física, mención Física-Matemática*, Universidad de Antofagasta, Chile, and acknowledges the support of ANID doctoral fellowship no. 21252201.

Appendix A: Pulse-level implementation of gate-based circuits

Quantum algorithms are implemented using quantum circuits composed of quantum gates. In superconducting quantum processors, these gates are realized through the precise control of electromagnetic pulses applied to the circuits. In platforms such as those developed by IBM, the hardware typically relies on a fixed set of quantum gates, each associated with predefined pulse shapes. Within these control schemes, cross-resonance pulses [17, 18, 37] are employed to mediate interactions between pairs of superconducting circuits. Despite their effectiveness, such gates are susceptible to various sources of error, including crosstalk, leakage to non-computational states, and decoherence effects [18, 38]. To mitigate these limitations, alternative pulse schemes, such as echo cross-resonance (ECR) [29], have been extensively studied. The following figures show the quantum gates schemes that represented the basic structure to build the pulses schemes defined in this work. Here, we considered native gates from the IBM_sherbrooke quantum hardware.

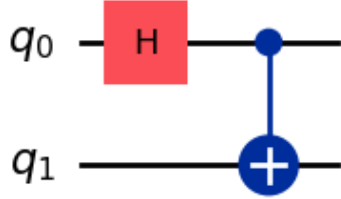


Figure 14. Circuit representation for Bell state $|\Psi\rangle = \frac{1}{\sqrt{2}}(|00\rangle + |11\rangle)$, this is obtained with Hadamard gate and CNOT gate, where q_0 is the control qubit and q_1 is the target qubit.

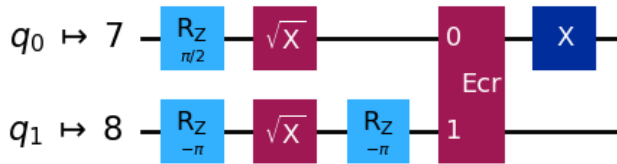


Figure 15. The representation of the transpiled figure (14) in the native gates of the IBM_sherbrooke simulator. Qubit seven is the control qubit, and qubit eight is the target qubit. For this case, a 2912 dt pulse scheme is needed

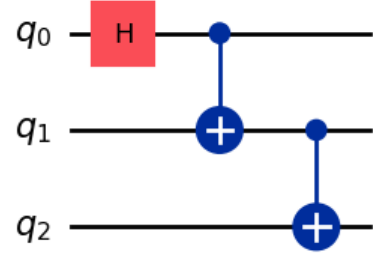


Figure 16. Representation of the GHZ state $|GHZ\rangle = \frac{1}{\sqrt{2}}(|000\rangle + |111\rangle)$ in a quantum circuit diagram. The state is obtained by implementing a Hadamard gate on q_0 and two consecutive CNOTs gates on qubits q_0 to q_1 and q_1 to q_2 respectively.

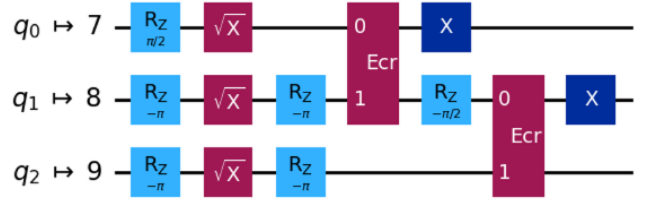


Figure 17. Representation of the circuit in figure (16) using the native gates of the IBM_sherbrooke simulator. This diagram shows two bipartite gates. To reproduce this state, the pulse sequence has a duration of 5312 dt

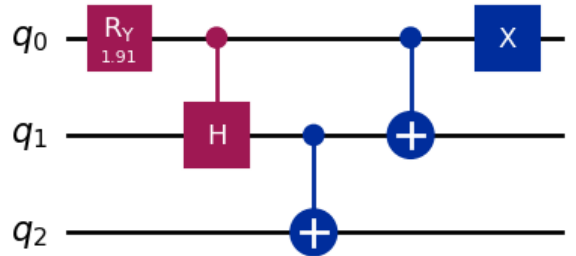


Figure 18. Representation of state $|W\rangle = \frac{1}{\sqrt{3}}(|100\rangle + |010\rangle + |100\rangle)$ in a quantum circuit scheme, on this occasion a R_Y gate and a Hadamard control gate, two CNOTs, and a Not gate are represented.

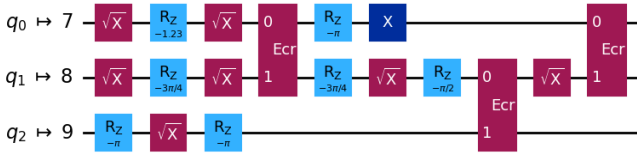


Figure 19. Representation of the scheme of figure (18) in the native gates of the IBM_sherbrooke simulator, it can be noted that there are three bipartite gates interleaved. The duration of this circuit is given by 8224 dt.

Each gate represents a pulse sequence that acts on some of the qubits, which change their energy state upon interacting with the pulse. Local gates are implemented with a single pulse, while bipartite gates like the ECR are implemented with a sequence of up to five pulses. In this research, the implemented sequences are based on the transpiled circuit in figures 15, 17 and 19.

It is worth noting that the times required to reproduce the pulses obtained for the schemes studied in our research are shorter than those given by default in the simulator, see Figures 1, 7, and 11. This is within the context of the fact that no decoherence was considered in this work. However, the parameters can serve as a guide for considering this approach, since some qubits may exhibit longer coherence times than our pulse scheme.

Appendix B: Electromagnetic pulse modeling and envelope functions

The quantum circuits used to create the states of interest in the research and the conversion to native gates of a quantum computer have been shown, but in reality these boxes are physically electromagnetic pulses; these pulses have a frequency and are modulated by means of a function that has certain parameters.

In the Hamiltonian control section of equations 3, 6, and 8, the function $\mu_i(t)$ is considered the envelope function, which must comply with certain restrictions. Furthermore, the implementation of this function depends on the wave generator used in the quantum computer hardware [39]. For example, for the simulator and the IBM_Sherbrooke computer, Gaussian, Gaussian_square, drag, and constant functions can be implemented [40].

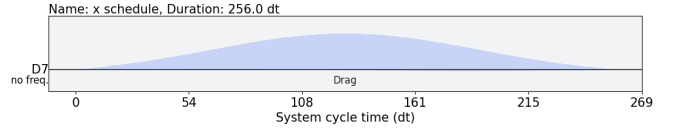


Figure 20. The envelope function used to produce the quantum gate X on the IBM_sherbrooke computer, this function is known as DRAG and consists of five parameters for its implementation.

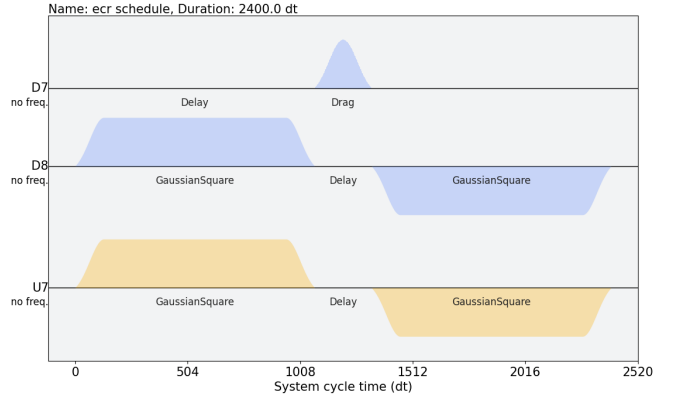


Figure 21. Pulse scheme for replicating the ECR quantum gate of the IBM_Sherbrooke computer. The sequence consists of five pulses, where qubit seven is the control qubit and qubit eight is the target. Implementation requires a drag function (see top line) and four square Gaussian functions.

The preceding graphs illustrate how quantum gates are implemented in pulse schemes. These functions are modulated by a cosine function, which must have the frequency of the qubit being controlled. Controlling the parameters of the envelope functions allows us to construct the desired quantum gates. However, for bipartite gates, extra pulses are necessary because the interaction between the qubits is somewhat more complex. For our implementation, we first used constant pulses as an evaluation of the desired states, and then we used more realistic pulses such as square Gaussian pulses, since they behave similarly to square pulses [41].

-
- [1] R. Chakrabarti and H. Rabitz, *Quantum control for scientists and engineers* (Princeton University Press, 2004).
- [2] K. Liu, *Optimal and robust quantum control in low dimensional systems*, Ph.D. thesis, Université Bourgogne Franche-Comté (2020).
- [3] C. P. Koch, U. Boscain, T. Calarco, G. Dirr, S. Filipp, S. J. Glaser, R. Kosloff, S. Montangero, T. Schulte-Herbrüggen, D. Sugny, and F. K. Wilhelm, Quantum optimal control in quantum technologies: Strategic report on current status, visions and goals for research in europe, *EPJ Quantum Technol.* **9**, 19 (2022).
- [4] P. Krantz, M. Kjørgaard, F. Yan, T. P. Orlando, S. Gustavsson, and W. D. Oliver, A quantum engineer's guide to superconducting qubits, *Appl. Phys. Rev.* **6**, 021318 (2019).
- [5] M. Ringbauer, M. Meth, L. Postler, R. Stricker, R. Blatt, P. Schindler, and T. Monz, A universal qudit quantum processor with trapped ions, *Nat. Phys.* **18**, 1053 (2022).
- [6] A. Castro, A. García Carrizo, S. Roca, D. Zueco, and F. Luis, Optimal control of molecular spin qudits, *Phys. Rev. Applied* **17**, 064028 (2022).
- [7] Z. Zhang, J. Ran, F. Gao, C. Jia, and X. Guo, Operation of single-spin qubits: Recent advances and prospects (adv. phys. res. 4/2025), *Advanced Physics Research* **4**, 2570010 (2025).
- [8] L. Henriët, L. Béguin, A. Signoles, T. Lahaye, A. Browaeys, G.-O. Reymond, and C. Jurczak, Quantum computing with neutral atoms, *Quantum* **4**, 327 (2020).
- [9] F. K. Wilhelm, S. Kirchhoff, S. Machnes, N. Wittler, and D. Sugny, An introduction into optimal control for quantum technologies, arXiv (2020), arXiv:2003.10132.
- [10] S. G. Schirmer and P. de Fouquieres, Efficient algorithms for optimal control of quantum dynamics: the "krotov" method unencumbered, *New Journal of Physics* **13**, 073029 (2011).
- [11] L. M. Fabra Martinez, *Control cuántico en dinámica coherente asistida por pinn y su resistencia a la disipación en dinámicas abiertas*, Ph.D. thesis, Universidad de Córdoba (2025).
- [12] Q. Ansel, E. Dionis, F. Arrouas, B. Peaudcerf, S. Guérin, D. Guéry-Odelin, and D. Sugny, Introduction to theoretical and experimental aspects of quantum optimal control, *J. Phys. B: At. Mol. Opt. Phys.* **57**, 133001 (2024).
- [13] R. Malarchick, Verified implementation of grape pulse optimization for quantum gates with hardware-representative noise models, arXiv (2025), arXiv:2511.12799.
- [14] S. Machnes, E. Assémat, D. Tannor, and F. K. Wilhelm, Tunable, flexible, and efficient optimization of control pulses for practical qubits, *Phys. Rev. Lett.* **120**, 150401 (2018).
- [15] Z. Wang, Quantum control based on deep reinforcement learning, arXiv preprint arXiv:2212.07385 (2022).
- [16] É. Genois, N. J. Stevenson, N. Goss, I. Siddiqi, and A. Blais, Quantum optimal control of superconducting qubits based on machine-learning characterization, *Phys. Rev. Applied* **24**, 034073 (2025).
- [17] J. George Francis and A. Shaji, Data-driven hamiltonian correction for qubits for design of gates, arXiv preprint arXiv:2505.02679 (2025).
- [18] H. N. Nguyen, F. Motzoi, M. Metcalf, K. B. Whaley, M. Bukov, and M. Schmitt, Reinforcement learning pulses for transmon qubit entangling gates, *Mach. Learn.: Sci. Technol.* **5**, 025066 (2024).
- [19] Y. Wang, Y. Ding, F. A. Cárdenas-López, and X. Chen, Pulse-based variational quantum optimization and meta-learning in superconducting circuits, *Physical Review Applied* **22**, 024009 (2024).
- [20] Z. Holmes, K. Sharma, M. Cerezo, and P. J. Coles, Connecting ansatz expressibility to gradient magnitudes and barren plateaus, *PRX Quantum* **3**, 010313 (2022).
- [21] M. Larocca, S. Thanasilp, S. Wang, K. Sharma, J. Biamente, P. J. Coles, L. Cincio, J. R. McClean, Z. Holmes, and M. Cerezo, Barren plateaus in variational quantum computing, *Nature Reviews Physics* , 1 (2025).
- [22] R. de Keijzer, O. Tse, and S. Kokkelmans, Pulse-based variational quantum optimal control for hybrid quantum computing, *Quantum* **7**, 908 (2023).
- [23] F. Platzer, F. Mintert, and A. Buchleitner, Optimal dynamical control of many-body entanglement, *Phys. Rev. Lett.* **105**, 020501 (2010).
- [24] F. Lucas, F. Mintert, and A. Buchleitner, Tailoring many-body entanglement through local control, *Phys. Rev. A* **88**, 032306 (2013).
- [25] S. A. Hill and W. K. Wootters, Entanglement of a pair of quantum bits, *Phys. Rev. Lett.* **78**, 5022 (1997).
- [26] X. Wei, J. Jiang, W. Xu, T. Guo, K. Zhang, Z. Li, T. Zhou, Y. Sheng, C. Cao, G. Sun, and P. Wu, Compact superconducting transmon qubit circuits made of ultrathin nbn, *Appl. Phys. Lett.* **123** (2023).
- [27] J. Kang, C. Kim, Y. Kim, and Y. Kwon, New design of three-qubit system with three transmons and a single fixed-frequency resonator coupler, *Sci. Rep.* **15**, 12134 (2025).
- [28] J. Koch, T. M. Yu, J. Gambetta, A. A. Houck, D. I. Schuster, J. Majer, A. Blais, M. H. Devoret, S. M. Girvin, *et al.*, Charge-insensitive qubit design derived from the cooper pair box, *Phys. Rev. A* **76**, 042319 (2007).
- [29] N. Sundaresan, I. Lauer, E. Pritchett, E. Magesan, P. Jurcevic, and J. M. Gambetta, Reducing unitary and spectator errors in cross resonance with optimized rotary echoes, *PRX Quantum* **1**, 020318 (2020).
- [30] M. AbuGhanem, Ibm quantum computers: Evolution, performance, and future directions, *J. Supercomput.* (2025).
- [31] W. Dür, G. Vidal, and J. I. Cirac, Three qubits can be entangled in two inequivalent ways, *Phys. Rev. A* **62**, 062314 (2000).
- [32] K. Coffman and Wootters, Distributed entanglement, *Phys. Rev. A* (2000).
- [33] Z. Liang, Z. Song, J. Cheng, Z. He, J. Liu, H. Wang, R. Qin, Y. Wang, S. Han, X. Qian, and Y. Shi, Hybrid gate-pulse model for variational quantum algorithms, in *Proc. ACM/IEEE Design Automation Conference (DAC)* (2023) pp. 241–256.
- [34] E. H. Hansen, X. Li, D. T. Chen, V. Kulkarni, *et al.*, Pulse-level variational quantum algorithms for molecular energy calculations using quansle, in *Proc. 32nd Int. Symp. High-Performance Parallel and Distributed Computing (HPDC)* (2023) pp. 241–256.
- [35] D. J. Egger, C. Capecchi, B. Pokharel, P. K. Barkoutsos,

- L. E. Fischer, L. Guidoni, and I. Tavernelli, Pulse variational quantum eigensolver on cross-resonance-based hardware, *Phys. Rev. Research* **5**, 033159 (2023).
- [36] K. M. Sherbert, H. Amer, and S. E. Economou, Parametrization and optimizability of pulse-level variational quantum eigensolvers, *Phys. Rev. Applied* **23**, 024036 (2025).
- [37] L. E. Fischer, A. Chiesa, F. Tacchino, D. J. Egger, S. Carretta, and I. Tavernelli, Universal qudit gate synthesis for transmons, *PRX Quantum* **4**, 030327 (2023).
- [38] R. Gautier, É. Genois, and A. Blais, Optimal control in large open quantum systems: The case of transmon readout and reset, *Phys. Rev. Lett.* **134**, 070802 (2025).
- [39] E. S. Matekole, Y.-L. L. Fang, and M. Lin, Methods and results for quantum optimal pulse control on superconducting qubit systems, in *Proc. IEEE Int. Parallel Distrib. Process. Symp. Workshops (IPDPSW)* (2022) pp. 600–606.
- [40] T. Alexander, N. Kanazawa, D. J. Egger, L. Capelluto, C. J. Wood, A. Javadi-Abhari, and D. C. McKay, Qiskit pulse: Programming quantum computers through the cloud with pulses, *Quantum Sci. Technol.* **5**, 044006 (2020).
- [41] Y. Zhu, J. Cheng, B. Li, K. Liu, Y. Zhou, H. Wang, Y. Ding, and Z. Liang, Hardware-aware calibration protocol for quantum computers, in *Proc. 52nd Annu. Int. Symp. Comput. Archit. (ISCA)* (2025) pp. 241–256.